Journal of Nondestructive Evaluation (2021) 40:59
https://doi.org/10.1007/s10921-021-00791-9

Determination of Carbon Steel Bar Diameter by Nondestructive Magnetic Testing

Aldecira G. Diogenes[1] · Elineudo P. de Moura[1] · André S. Machado[1] · Lindberg L. Gonçalves[1,2]

Received: 17 August 2020 / Accepted: 11 June 2021 / Published online: 25 June 2021

Abstract
Carbon steel is an important component in reinforced concrete structures. These composite materials are susceptible to various degradation processes, especially the corrosion of steel bars. Since they play an important role in the stability of reinforced concrete structures, these structures require periodic inspections to verify their physical conditions. Therefore, a nondestructive testing technique is proposed that is based on electromagnetic induction, which is capable of discriminating the diameters of steel bars. This technique was simulated with the COMSOL Multiphysics software and experimentally tested in the laboratory. Magnetic hysteresis loops were obtained for steel bars with 5.0, 6.3, 8.0, and 10.0 mm diameters at 0, 10, and 20 mm depths for sinusoidal and triangular excitation fields. The results obtained from the hysteresis loops for the maximum values of the field, remanence, and coercivity were processed by principal component analysis, Karhunen–Loéve transformation, Gaussian classifier, and artificial neural network. The confusion matrices produced by these pattern recognition techniques were analyzed, and the results show that the proposed method can distinguish different steel bar diameters, but is limited to a maximum depth.

Keywords Nondestructive testing · Magnetic methods · Carbon steel bar · Electromagnetic sensor · Pattern classification techniques

1 Introduction

Carbon steel is a ferrous alloy in which the carbon content ranges from 0.10 to 1.00% and can present small quantities of other chemical elements. They are classified into the following groups according to their carbon content: low carbon steel with 0.10 to 0.25% C, medium carbon steel with 0.25 to 0.55% C, and high carbon steel with 0.55 to 1.00% C. These steel types can be quenched and tempered for increased strength. The addition of carbon and other alloy elements, such as Mn, Ni, Cr, Si, P, and Cu, to steel changes its mechanical properties (tensile strength, yield strength, and hardness, for example) [1].

✉ Aldecira G. Diogenes
aldeciragd@alu.ufc.br

[1] Graduate Program in Materials Science and Engineering, Department of Metallurgical and Materials Engineering, Universidade Federal do Ceará, Campus do Pici, Building 729, Fortaleza 60440-554, Brazil

[2] Campus de Russas da Universidade Federal do Ceará, Russas, Ceará 60900-000, Brazil

Carbon steels are widely used in civil construction as metal structures or reinforced concrete structures. In this work, we studied low carbon steel used in reinforced concrete structures (steel rebar) known as cold rolled steel, with a 5.0 mm diameter, and hot rolled steel, with 6.3, 8.0, and 10.0 mm diameters.

Due to their importance for the structural stability of concrete structures, these structures need to be inspected and tested during their life cycle to determine their health and to prevent disasters. Therefore, nondestructive techniques have been applied in the past years to evaluate the integrity of the components of concrete structures [2].

The magnetic response of ferromagnetic materials is affected by the manufacturing process, chemical composition, microstructure, ambient effects, mechanical stresses, and degradation phenomena in materials, such as creep, fatigue, and corrosion [3, 4]. In recent decades, magnetic methods have been applied to reinforced concrete structures to acquire information about the state of the ferromagnetic material embedded in the concrete. Among these methods, determination of the hysteresis loops plays an important role since their main characteristic parameters, namely,

remanence, coercivity, and permeability, are sensitive to stress and strain, grain size, and other properties. Other magnetic methods, such as eddy currents and magnetic flux, can be applied to find voids, cracks, and corrosion [4].

In particular, magnetic methods, such as remanent magnetic field, have been applied to single prestressing steel bars to localize fractures [5, 6]. Magnetic flux leakage was used in ferromagnetic plates to determine internal and external defects [7] and in tendons present in prestressed concrete structures to detect ruptures [8]. Also, an induced magnetic flux was applied to detect corrosion in embedded prestressing strands [9, 10].

In most applications of the magnetic techniques in ferromagnetic materials, the magnetic response is expressed in terms of magnetization curves or families of hysteresis loops [11]. The magnetic properties of carbon steel rods have also been used for microstructure identification [12], detection of their corrosion state [3], and in mild steel, for characterization of the degradation in the elastic range [13].

The ferromagnetic materials may be described in terms of domains, introduced by Weiss [14], in which the magnetic materials are made up of several microscopic magnetic domains. The domains of an unmagnetized magnetic sample are arranged such that there is no net magnetic moment. It means that all the domains are individually saturated, and their orientation is random, i.e., in different directions; therefore, the net magnetization is zero because the magnetization vectors cancel each other out. However, when a magnetic field is applied in a ferromagnetic material, the domains rotate and align in the direction of the applied magnetic field, and consequently, a nonzero magnetization is induced in the material [15].

Since reinforced concrete structures are susceptible to various degradative processes, especially corrosion of the steel components, these structures require periodic nondestructive inspections to obtain reliable and accurate information about their components' physical conditions to avoid their collapse. Therefore, this work aims to investigate the feasibility of nondestructive electromagnetic testing performed with a simple prototype sensor for discriminating the diameter of carbon steel bars in concrete at different depths.

The magnetic method applied is based on Faraday's Law of electromagnetic induction. An electric current or voltage induced in the pickup coil of the sensor due to an alternating current applied in the driver coil, both placed around a ferromagnetic yoke, is the working principle of this experiment, and, in this work, we have considered that the applied voltage variation followed sinusoidal and triangular waveforms. To determine the hysteresis, we have also used Ampere's Law. The sensor and rebar have been modeled using COMSOL Multiphysics software.

The magnetic responses obtained from the hysteresis loops, namely, remanence, coercivity, and maximum values of the applied and induced fields, have been analyzed considering the mean and standard deviation of their statistical distributions. They have also been analyzed using the pattern classification algorithms: principal component analysis, Karhunen–Loéve transformation, Gaussian classifier, and artificial neural network. These algorithms were implemented using MATLAB software.

2 Materials and Methods

2.1 Samples

Two commercial steel bars used in concrete structures known as cold-rolled (5.0 mm diameter) and hot-rolled rebars (6.3, 8.0, and 10.0 mm diameters) were used in this study. The samples are about 1000 mm long. The magnetic response for each sample was determined from the hysteresis curves (Fig. 1). The purpose of using different rebar diameters was to evaluate the change in their magnetic response by the hysteresis loops.

Figure 1 illustrates a typical hysteresis loop for evaluating the behavior of a ferromagnetic sample, where B_s stands for the saturation flux density corresponding to the magnetic field strength H, B_r is the remanence or remanent flux density, and H_c is the coercivity or coercive force.

In this work, for the hysteresis loops obtained for each rebar, we have used the coercivity, H_c, remanence, B_r, maximum flux density, B_{max}, and their corresponding maximum magnetic field strength, H_{max}, to characterize each rebar state.

2.2 Experiment Description

Figure 2 shows a diagram of the experimental device. The experiment consists of a waveform generator (Keithley 3390), a bipolar power supply (Kepco, BOP 20-20 D), an

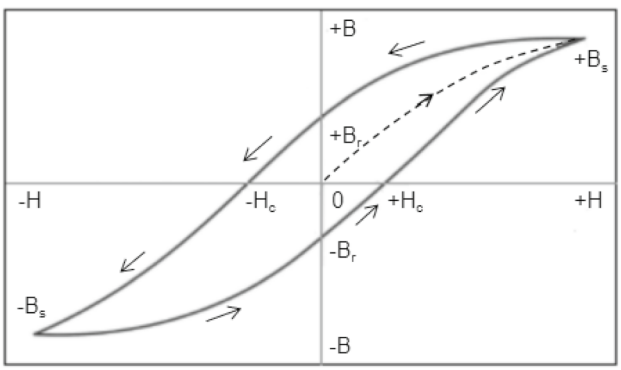

Fig. 1 Hysteresis loop for a ferromagnetic

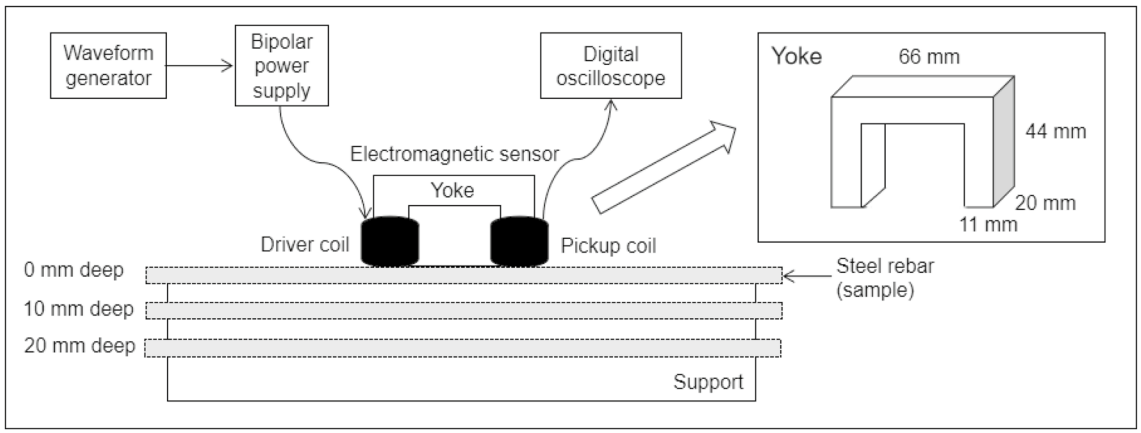

Fig. 2 Diagram of the experimental device. Dimensions are in millimeters

electromagnetic sensor, and a digital oscilloscope (Agilent Technologies, DSO9104A0).

The prototype sensor was developed in the Center for Nondestructive Evaluation (CENDE) of the Federal University of Ceará. The sensor consists of two coils (one driver and one pickup) encircling a ferromagnetic yoke. The yoke is built with 40 silicon steel laminas, each with a 0.5 mm width, and its final dimensions are 66 mm long, 44 mm high, and each of its legs is 20 mm wide. The laminated silicon steel was chosen in order to reduce the losses due to eddy currents and because the material is adequate for low frequency excitations. Each coil (or solenoid) has 600 turns of copper wire (0.511 mm diameter). The depths (to simulate the concrete) were adjusted using 10 mm thick wood plates positioned over the rebars.

The waveform generator feeds the power supply by sending excitation signals. Sinusoidal and triangular waveforms at a low frequency of 5 Hz and a voltage of 10 V were used in this study to reduce the flux losses. Since the losses depend on the waveform of the excitation [16], two waveforms were used in order to improve the resolution of the hysteresis curve. For each diameter and each depth, thirty measurements around the middle of the rebars were recorded. The electromagnetic sensor (sensor/probe/yoke) was placed over the sample and aligned to its length. Alternating current was applied to the driver coil that magnetizes the rebar, and the pickup coil reads the magnetic flux changes.

The data were read with the help of the Agilent graphical program implemented in the data acquisition of the oscilloscope. The signals collected from each rebar were processed by using MATLAB software to plot the hysteresis curves. The magnetic hysteresis loops (B = f(H)) were plotted in S.I. units. For each rebar, at different depths, features such as the magnetization maximum, the remanence, and the coercivity were extracted from the hysteresis loops and recorded.

2.3 Simulation Model

The electromagnetic sensor was modeled with the COMSOL Multiphysics software and was evaluated by comparing their response to the experimental measurements. This sensor has two coils physically separated from each other and are located on two different portions of the yoke.

The COMSOL Multiphysics platform, in the AC/DC module, provides a variety of resources for investigating electromagnetic fields. The 3D model was built using the Magnetic Fields and Electric Circuit physics interfaces of the AC/DC Module and Preset Studies for Selected Physics. The geometry of the model and parameter definitions were created based on the experimental data.

Materials with electrical properties were chosen for the computational modeling of the coil and yoke. The steel rebar material was chosen from the nonlinear magnetic materials list of the COMSOL for low carbon steel [17]. In Fig. 3, we show the B-H relationship used for cold and hot rolled steel rebar material, and, as depicted in the figure, no significant difference is present in the curves. Consequently, we assumed that the results do not depend on the rolling process.

The relative permeability and relative permittivity of copper used in the computational modeling of the coil conductor were defined as equal to one, and the yoke relative permeability was defined as equal to 7,000 [18]. The B-H relationship used for the yoke material**,** as calculated by COMSOL, is shown in Fig. 4.

All the subfields of physics interface of Magnetic Field and Electric Circuit were chosen as described elsewhere [19]. The conductivity and the cross-sectional area of the coil wire were defined as 5.8×10^7 S/m and 0.205×10^{-6} m^2, respectively [20]. After defining the physics interface for the model, the next step in the modeling was to define the mesh. User-controlled mesh and Finer element size for

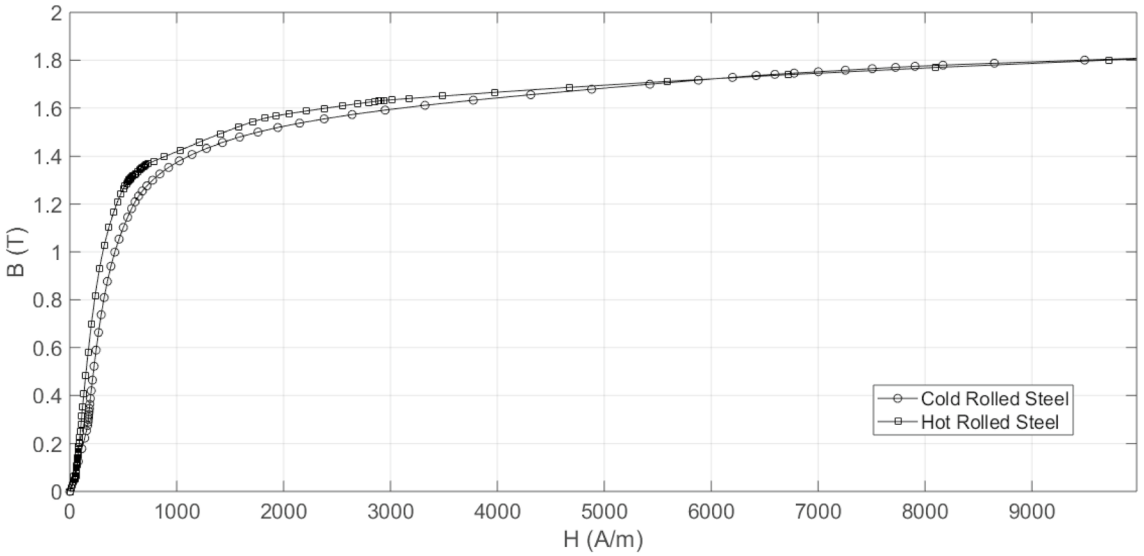

Fig. 3 B-H relationship for cold and hot rolled steel rebars

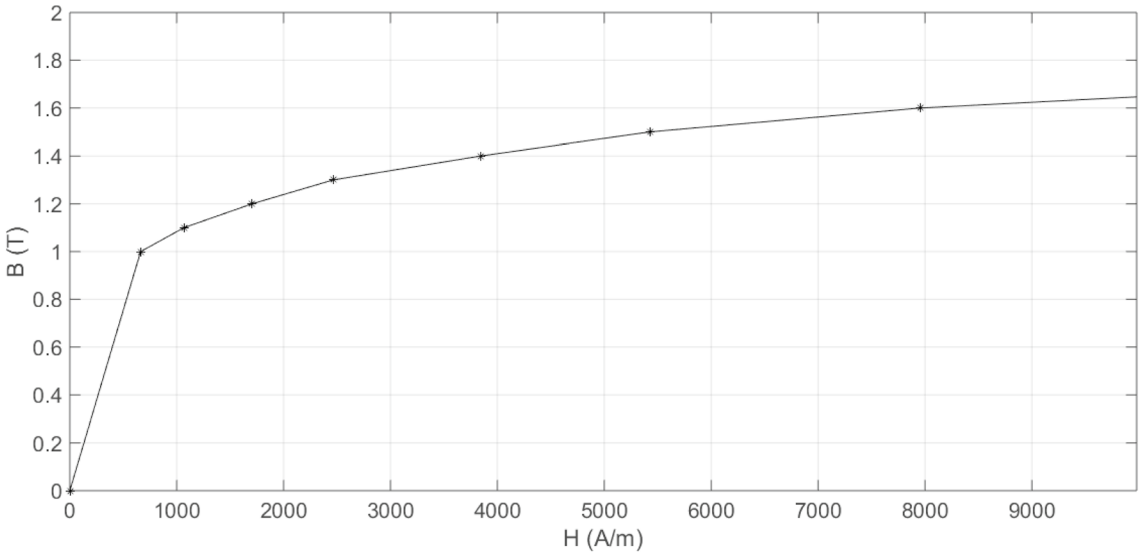

Fig. 4 B-H relationship for the yoke

unstructured triangular mesh were selected, and a maximum of 121,682 tetrahedral finite elements were used. It should be noticed that no significant modification to the results was observed by using Extra fine element size, and the minimum size of the mesh element was 4.32 mm. Figure 5 shows the final geometry and mesh for the electromagnetic sensor.

2.4 Data Analysis

A signal with the voltage variation measured in the pickup coil was recorded for each steel rebar. Thirty measurements were recorded around the middle of the rebar for different rebar diameters and depths. All the experimental hysteresis loops were acquired and recorded with 201 points at a sample rate of 1000 samples/s.

The remanence, B_r, coercivity, H_c, maximum flux density, B_{max}, and maximum magnetic field, H_{max}, were obtained from the hysteresis loops for each rebar. The mean values and standard deviations for each were determined. Also, the data input and the classification were organized according to the diameters of the bar (5.0, 6.3, 8.0, and 10.0 mm), independently of its depth (0, 10, and

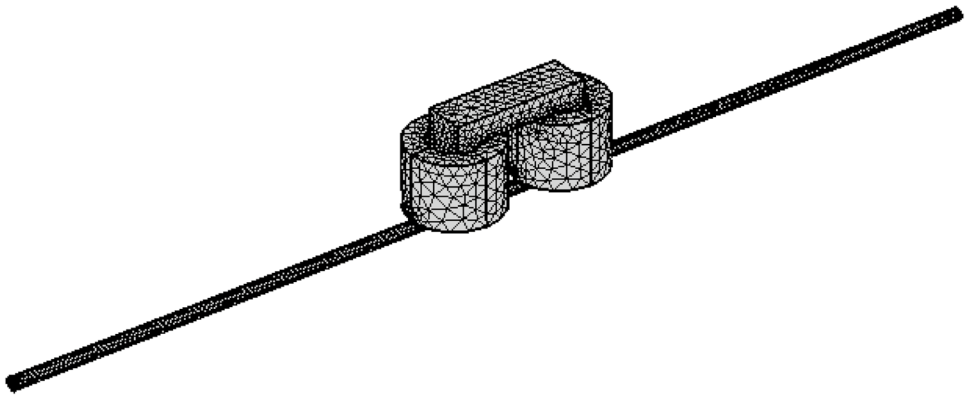

Fig. 5 Geometry and mesh 3D simulation model

20 mm), which resulted in four classes. Each data has four attributes (B_r, H_c, B_{max}, and H_{max}).

These classes were classified using pattern recognition techniques, such as principal component analysis (PCA), Karhunen–Loéve (KL) transformation, Gaussian classifier, and artificial neural network [21].

All data were normalized before the pattern recognition analysis. The supervised learning algorithms (KL transformation, Gaussian classifier, and neural network) used 100 random training and test sets for each class. The training set was built by selecting 80% of the data, while the 20% remaining was used to define the testing set, except for PCA, which used 100% of the data. All confusion matrices presented are averages calculated over the 100 distinct choices of training and testing sets. The purpose of the test data is to evaluate the classifier's performance for data that were not used during the training set. The PCA and KL classifiers use the Euclidean distance and the nearest-class-mean rule to the first two principal components of the training or testing data.

2.5 Pattern Recognition Techniques

Pattern recognition uses classification or clustering algorithms through pattern observations based on a set of characteristics. They can be divided into supervised (train classifier) and unsupervised (clustering). The pattern recognition techniques used in this work are PCA (an unsupervised algorithm), Karhunen–Loéve transformation (a supervised algorithm), Gaussian classifier (a supervised algorithm), and artificial neural network (it can be either supervised or unsupervised). Here, a neural network with an error back-propagation learning algorithm was used.

We have assumed that the input data is arranged in a m x n matrix $\mathbf{X}$, where m is the number of signals produced (columns) and n is the number of dimensions of each signal (rows). Each column of $\mathbf{X}$ represents an observation $\mathbf{x}_i$ (variable) corresponding to the i-th signal.

2.5.1 Principal component analysis

Principal component analysis is defined in the paper by Webb [21]. First, the covariance matrix $\mathbf{S}$ is built and given by

$$\boldsymbol{S} = \frac{1}{n}\sum_{i=1}^{n}(\boldsymbol{x}_i - \bar{\boldsymbol{x}}_i)^T \tag{1}$$

and

$$\bar{\boldsymbol{x}} = \frac{1}{n}\sum_{i=1}^{n}\boldsymbol{x}_i \tag{2}$$

where $\bar{\boldsymbol{x}}$ is the average of the variables of matrix $\mathbf{X}$ and T represents the transposed vector.

The eigenvalues and eigenvectors of $\mathbf{S}$ are calculated, and the eigenvectors are arranged in decreasing order in matrix form, defined as the transformed matrix, associated with their eigenvalue values. Thus, their principal components are defined.

2.5.2 Karhunen–Loéve Transformation

The Karhunen–Loéve transformation projects the training vectors $\mathbf{x}_i$(columns) along the eigenvectors of the within-class covariance matrix, $\mathbf{S}_w$, and rescales the resulting vectors by a diagonal matrix constructed from the eigenvalues of $\mathbf{S}_w$. Finally, the resulting vectors are projected onto the eigenvectors of the between-class covariance matrix, $\mathbf{S}_B$. The full transformation can be written as described elsewhere [21–24].

2.5.3 Gaussian Classifier

The general p-dimensional Gaussian function for given class i is given by Webb [21]

$$p = \frac{1}{(2\pi)^{\frac{p}{2}}|\boldsymbol{S}|^{\frac{1}{2}}}\exp\left[-\frac{1}{2}(\boldsymbol{x}-\bar{\boldsymbol{x}})^T\boldsymbol{S}^{-1}(\boldsymbol{x}-\bar{\boldsymbol{x}})\right] \tag{3}$$

where $\mathbf{x}$ denotes an input training vector and T is the transposed vector. The mean vector $\bar{\mathbf{x}}$ and the covariance

matrix $\boldsymbol{S}$ of the Gaussian function is calculated for each class i, which in turn is given by Eqs. (1) and (2), respectively.

The Gaussian function has its maximum value when $\boldsymbol{x} = \overline{\mathbf{x}}$, and the increase in the distance between them decreases the output of the function. For the testing set, Gaussian classifier discrimination is done for each data, associating each vector to the class with the highest output [24].

2.5.4 Artificial Neural Networks

Artificial neural networks are composed of a set of mathematical operators called neurons. These neurons are arranged in layers, and the information stored in their synaptic weights during the learning process makes them able to map any mathematical functions. Therefore, artificial neural networks can be used as a classifier or regressor [25]. In the first step of the method, input signals x_i are added to the neuron and multiplied by the synapse weights (w_i), resulting in the sum. Then, bias (b) is added and sent to the activation function g, where it will allow the signal to pass or not (ϕ limits output between [0,1] in this work). Thus, this can be represented by an output y defined as

$$y = \phi\left(\sum_{i=1}^{n} w_i x_i + b\right) \tag{4}$$

There are many neural networks for pattern classification, such as a multilayer perceptron that was used in this work. This neural network is organized into layers, and it has unidirectional connections between them. The estimation process is divided into two main steps: training and testing. In the training step, the network is training with a set of input and output pairs so that synapse weights can be adjusted. In the testing step, the network is exposed to new data [24].

3 Results

Table 1 presents the nomenclature used to identify steel rebar diameters, independently of the depth.

In Fig. 6, we show typical experimental hysteresis curves for the steel rebars at 0 mm, 10 mm, and 20 mm depths for an externally applied magnetic field with a sinusoidal waveform.

Table 1 Nomenclature of classes of rebar diameters

Class	1	2	3	4
D (mm)	5.0	6.3	8.0	10.0

3.1 Simulation Results

The sensor and rebar were modeled with the COMSOL Multiphysics software. As already pointed out, this analysis was made based on four magnetic properties, such as remanence, B_r, coercivity, H_c, maximum flux density, B_{max}, and maximum magnetic field strength, H_{max}, obtained from the hysteresis loops. For the analysis of the simulation, 30 hysteresis loops were generated for each class and depth of the rebar such that the total dataset had 360 loops for each excitation waveform.

In Figs. 7 and 8, we show the mean value and standard deviation of these four features as a function of the rebar depth for an externally applied magnetic field with a sinusoidal and triangular waveform, respectively.

From the results shown in Fig. 7, taking into account the statistical fluctuations, we can conclude that, due to overlap of the values, a single magnetic feature cannot be used as a classifier capable of identifying the diameter at any depth of the bars. The same conclusion can also be reached from the results shown in Fig. 8.

Since any of the four magnetic features cannot be regarded as a suitable attribute for distinguishing the diameters, we considered a new set of data composed of four-dimensional vectors whose components were the four magnetic features of the hysteresis loops. Then, we analyzed the new dataset by using the classifiers PCA, KL transformation, Gaussian classifier, and artificial neural network.

The results obtained from PCA are shown in Table 2, where we have considered simultaneously all datasets obtained for the different diameters and depths since PCA is an unsupervised classifier. As it can be seen, PCA was able to identify two classes only, namely, classes 1 and 4, independently of the excitation waveform of the hysteresis loops.

To apply the supervised classifiers, namely, KL transformation, Gaussian classifier, and artificial neural network, as already pointed out, the dataset was divided into a training set with 80% of the vectors and a testing set with 20% testing vectors. To give robustness to the results, we applied the classifiers to 100 training and testing sets randomly generated from the original data.

In Tables 3 and 4, we show the percentage of data that was correctly classified in the training and testing stages by KL transformation, Gaussian classifier, and neural network for excitation with sinusoidal and triangular waveforms, respectively. The results are remarkably good considering that the overall average rate of success was above 97% for the different classifiers and excitation waveforms.

3.2 Experimental Results

A similar analysis applied to the simulation data was also applied to the experimental data obtained from the

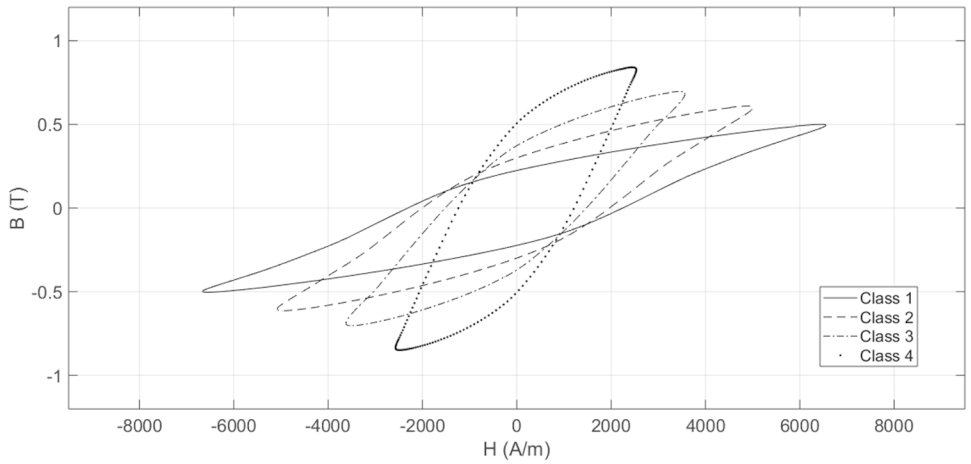

(a)

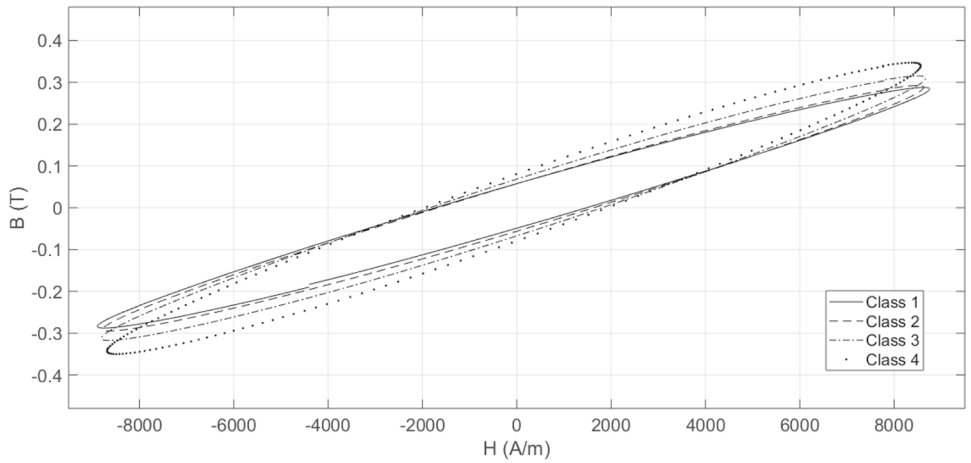

(b)

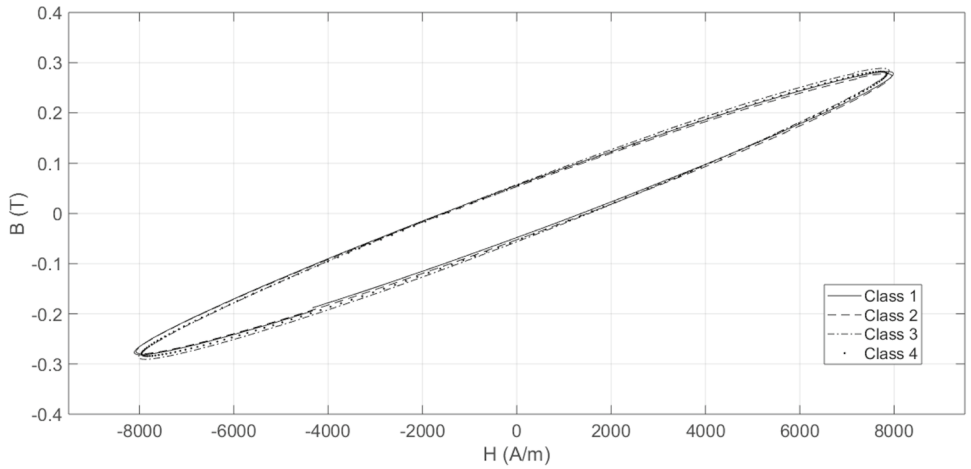

(c)

Fig. 6 Typical experimental hysteresis curves for the steel rebars at 0 mm (**a**), 10 mm (**b**), and 20 mm (**c**) depths

experimental hysteresis loops. For this analysis, as in the case of the simulation results, 30 hysteresis loops were obtained for each class and depth of the rebar such that the total dataset had 360 loops for each excitation waveform.

In Figs. 9 and 10, we present the mean value and standard deviation of the four magnetic features as a function of the rebar depth for an externally applied magnetic field with sinusoidal and triangular waveforms, respectively. With the

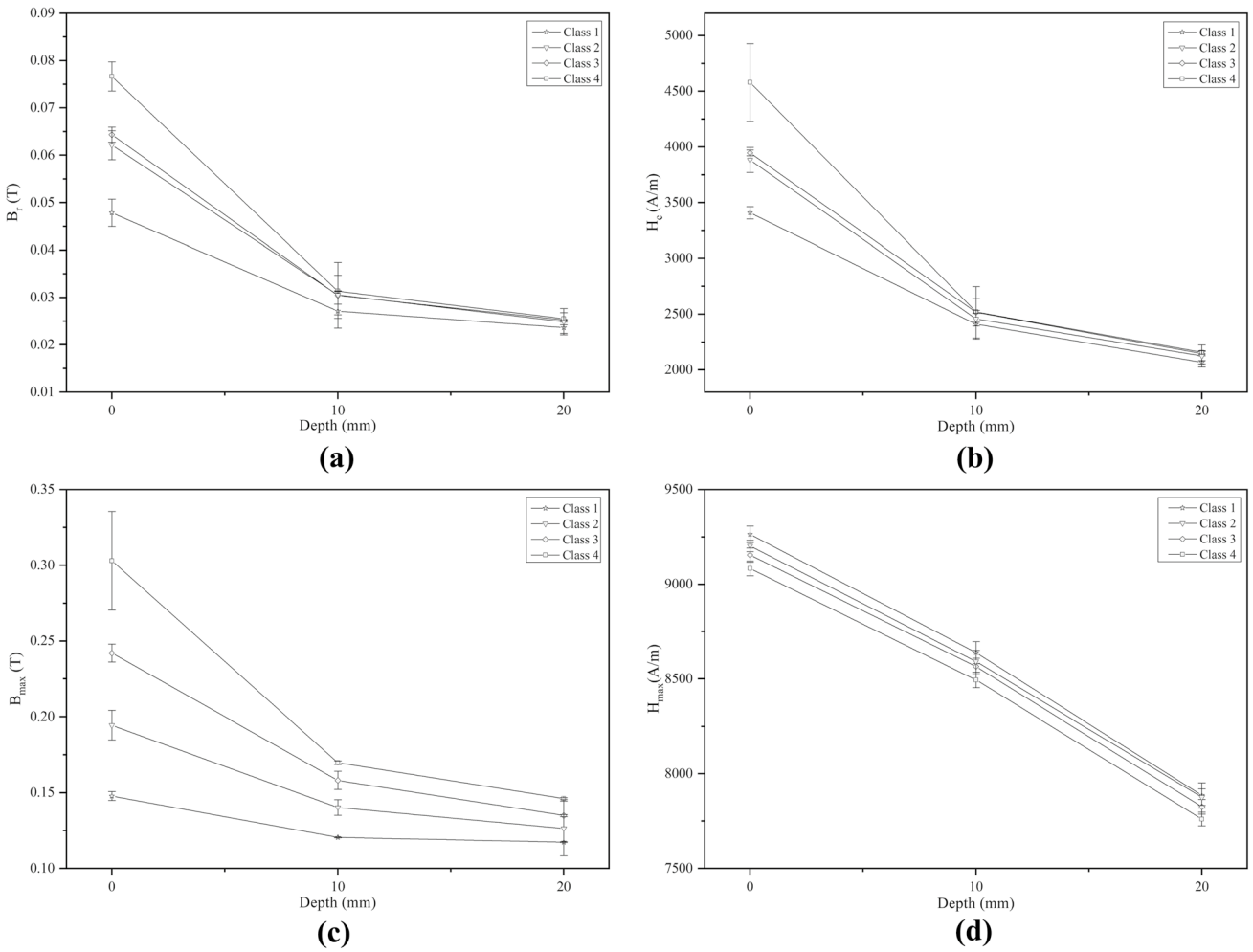

Fig. 7 The remanence (**a**), coercivity (**b**), maximum flux density (**c**), and maximum magnetic field strength (**d**) vs. the depth of the bars for an excitation magnetic field with a sinusoidal waveform (simulation results)

same number of experimental hysteresis loops, the results present the same behavior as the simulation results, which validate the measurement. Consequently, none of the magnetic features can be used as a classifier capable of identifying the diameter at any depth of the bars.

Thus, as in the previous case, we applied the same pattern recognition techniques for the experimental results. The vectors of the dataset to be analyzed were constructed in the same way with the four magnetic features obtained from the hysteresis loops.

The PCA results are shown in Table 5, which shows the percentage of experimental data that was correctly classified for the excitation magnetic field with sinusoidal and triangular waveforms. These results are identical to the ones obtained from the numerical simulation that are shown in Table 2.

Therefore, by using the identical procedure applied in the treatment of the simulation results, we applied the supervised classifiers to the experimental results by considering 100 randomly selected testing sets built with 80% of the data and 100 training sets built with the remain 20% of the data.

In Tables 6 and 7, we show the percentage of the training and testing vectors that were correctly classified by the supervised classifiers, KL transformation, Gaussian classifier, and neural network for training and testing vectors and excitation with sinusoidal and triangular waveforms, respectively. The results are in total agreement with the ones obtained for the simulation data. It should be noted that, for the triangular waveform, the success rate of the neural network classifier was almost 100%.

4 Discussion

We present the simulation results in Figs. 7 and 8, where we show the mean and standard deviation of the remanence, B_r, coercivity, H_c, maximum flux density, B_{max}, and magnetic field strength, H_{max}, for sinusoidal and triangular excitations

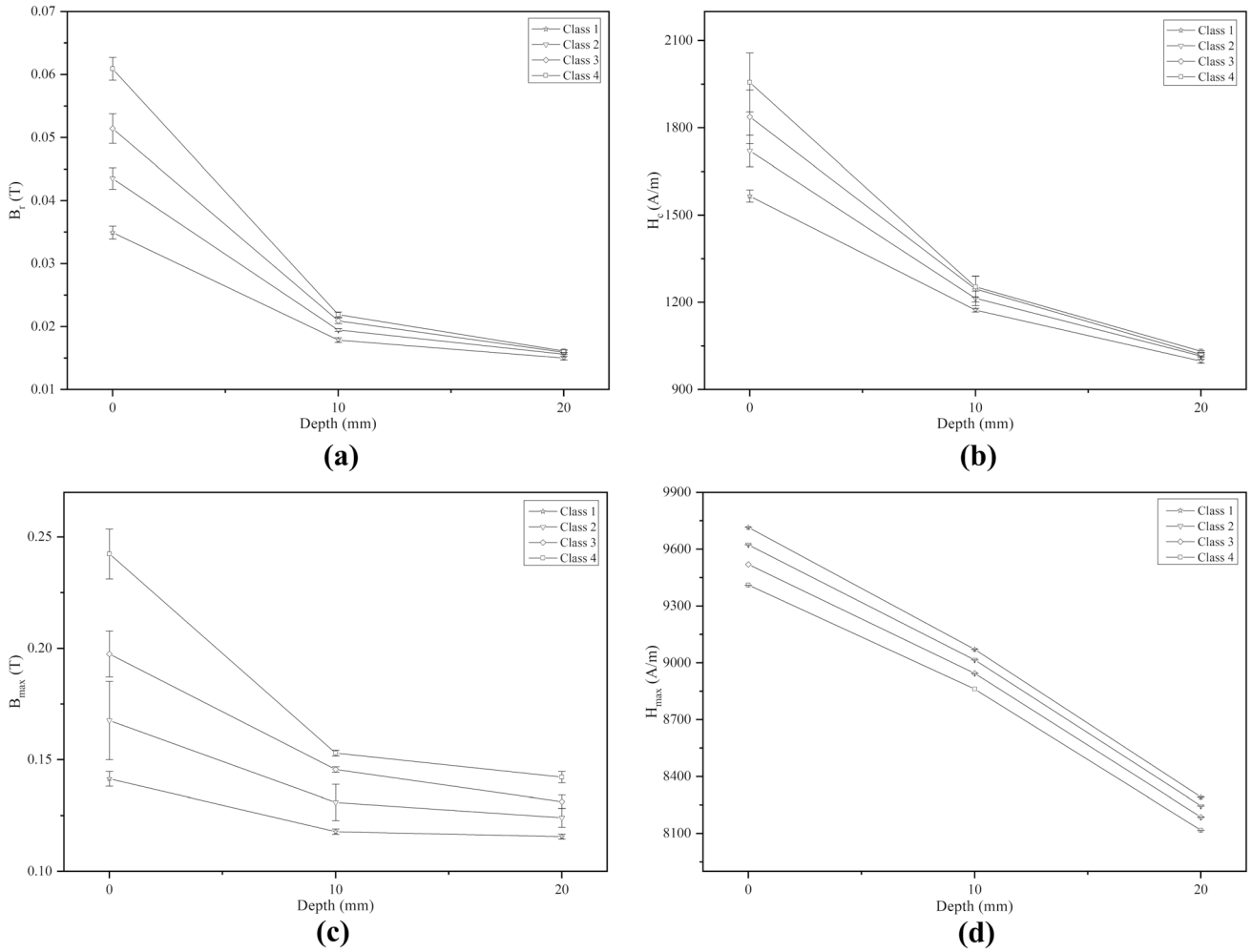

Fig. 8 The remanence (**a**), coercivity (**b**), maximum flux density (**c**), and maximum magnetic field strength (**d**) vs. the depth of the bars for an excitation magnetic field with a triangular waveform (simulation results

Table 2 Percentage of simulated data that was correctly classified by PCA

Class	Sinusoidal	Triangular
1	67	67
2	0	1
3	0	0
4	33	33
Overall average	25	25.25

used to assign magnetic properties extracted from simulated hysteresis loops obtained for the different rebar diameters. According to the figures, the results of B_r, H_c, B_{max}, and H_{max}, individually, were not able to discriminate the bar diameters at different depths.

The statistical parameters (mean and standard deviation) of the magnetic features extracted from experimental hysteresis loops (remanence, coercivity, maximum flux density, and magnetic field strength) reproduce essentially the same results obtained from the simulation results. Therefore, the data had to be analyzed by pattern recognition techniques. To this aim, the data was organized by rebar diameters, independently of its depth, and inserted in the classifiers.

In Tables 2, 3, and 4, we show the performance of the different classifiers (PCA, KL transformation, Gaussian, and neural network) for the computational results. The average success rates obtained by the unsupervised learning classifier PCA were 25% and 25.25% for external magnetization with sinusoidal and triangular waveforms, respectively, which was a very poor result. On the other hand, all the supervised classifier algorithms presented remarkably good results. The average success rates of the KL transformation algorithm were 98.5% (training set) and 97.75% (testing set) for an external excitation with sinusoidal waveform and

Table 3 Percentage of simulated data that was correctly classified for a sinusoidal waveform

Class	Karhunen–Loève		Gaussian		Neural network	
	Training	Testing	Training	Testing	Training	Testing
1	100	99	98	98	99	99
2	96	96	98	98	99	99
3	98	98	97	97	99	99
4	100	98	98	97	99	99
Overall average	98.5	97.75	97.75	97.5	99	99

Table 4 Percentage of simulated data that was correctly classified for a triangular waveform

Class	Karhunen–Loève		Gaussian		Neural network	
	Training	Testing	Training	Testing	Training	Testing
1	100	100	99	99	100	100
2	100	100	99	99	100	99
3	100	100	99	98	99	99
4	100	100	99	99	100	100
Overall average	100	100	99	98.75	99.75	99.5

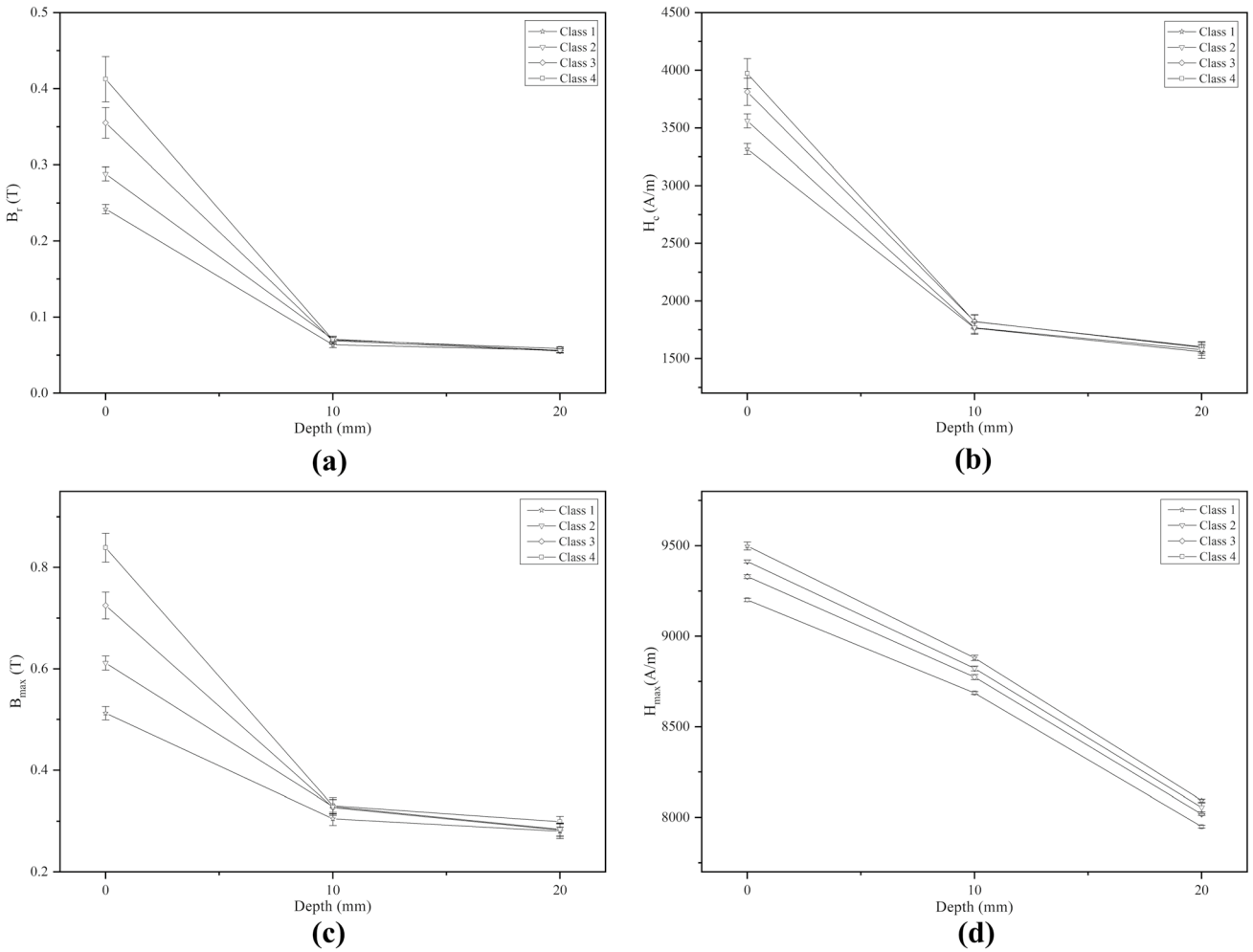

Fig. 9 The remanence (**a**), coercivity (**b**), maximum flux density (**c**), and maximum magnetic field strength (**d**) vs. the depth of the bars for an excitation magnetic field with a sinusoidal waveform (experimental results)

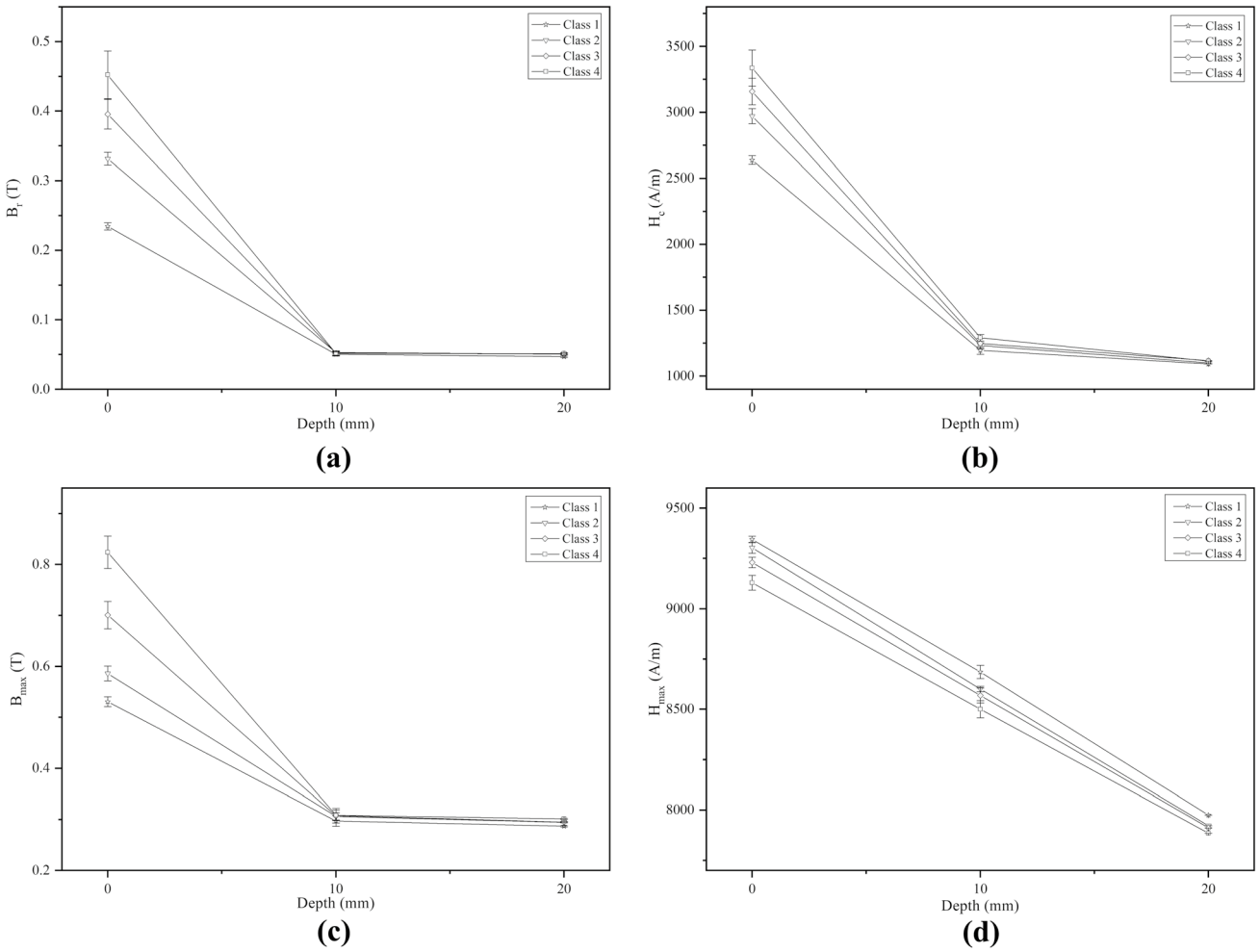

Fig. 10 The remanence (**a**), coercivity (**b**), maximum flux density (**c**), and maximum magnetic field strength (**d**) vs. the depth of the bars for an excitation magnetic field with a triangular waveform (experimental results)

Table 5 Percentage of experimental data that was correctly classified by PCA

Class	Sinusoidal	Triangular
1	67	67
2	0	1
3	0	0
4	33	33
Overall average	25	25.25

100% (training set) and 100% (testing set) for the triangular excitation, and the Gaussian classifier presented slightly different average success rates, with 97.75% (training set) and 97.5% (testing set) for a sinusoidal waveform and 99% (training set) and 98.75% (testing set) for the triangular waveform. The neural network achieved average success rates of 99% (training set) and 99% (testing set) for sinusoidal external excitation and 99.75% (training set) and 99.5% (testing set) for triangular excitation.

Table 6 Percentage of experimental data that was correctly classified for a sinusoidal waveform

Class	Karhunen–Loève		Gaussian		Neural network	
	Training	Testing	Training	Testing	Training	Testing
1	96	95	100	100	99	99
2	97	98	99	99	99	99
3	95	95	100	99	99	99
4	100	98	100	100	100	99
Overall average	97	96.5	99.75	99.5	99.25	99

Table 7 Percentage of experimental data that was correctly classified for a triangular waveform

Class	Karhunen–Loève		Gaussian		Neural network	
	Training	Testing	Training	Testing	Training	Testing
1	100	100	99	99	99	99
2	100	99	99	99	99	99
3	98	97	98	98	99	99
4	99	97	99	99	99	99
Overall average	99.25	98.25	98.75	98.75	99	99

In Figs. 9 and 10, we present the four magnetic features extracted from the experimental hysteresis loops produced with sinusoidal and triangular external excitations, respectively. As in the case of the numerical simulation, the results shown for B_r, $H_{c,}$ and B_{max} and H_{max} were not able to discriminate the diameters at the different depths.

It is also worthwhile pointing out that, although the experimental results are similar to those produced by the computational simulation, the error bars of the four features extracted were more significant when compared to the computational results.

In Table 5, we show the performance of the classifier based on PCA for grouping the features extracted from the experimental hysteresis loops according to rebar diameters, which achieved identical misclassification rates to the ones obtained for the simulated data. The overall success rates were only 25% and 25.25% for the experimental data obtained with sinusoidal and triangular magnetic strength.

The performance of the classifiers KL transformation, Gaussian classifier, and neural network for the experimental results can be found in Tables 6 and 7. For the sinusoidal magnetic strength in Table 6, the average success rates obtained with the KL classifier were 97% and 96.5% for training and testing, respectively, followed by the Gaussian classifier with 97.75% and 97.5%, and the neural network with 99.25% and 99%. The results presented in Table 7 for triangular magnetic strength show that average success rates of 99.25% and 98.25% were obtained using the KL classifier for training and testing, followed by the Gaussian classifier with 98.75% and 98.75% success rates, and finally the neural network with 99% and 99% success rates.

Finally, it is worth mentioning that, unlike PCA, all the supervised learning classifiers achieved high success rates in training and testing for both of the external excitation waveforms. Furthermore, the results indicate that the triangular excitation improves the performance of the classifiers.

5 Conclusions

For the computational and experimental results, the statistical parameters (mean and standard deviation) of the magnetic features extracted from the experimental hysteresis loops (remanence, coercivity, and maximum flux density) did not present significant changes to provide satisfactory discrimination of the rebar diameters.

For the computational results, the best average success rates for the four classifiers (PCA, KL transformation, Gaussian classifier, and neural network) were obtained using the neural network (with 99% success for training and testing, respectively), followed by KL transformation (with 98.5% and 97.75%), Gaussian classifier (with 97.75% and 97.5%), and PCA (with 25%) for an external excitation with a sinusoidal waveform. As for the triangular waveform, the best average success rates were obtained using KL transformation (with 100% success for training and testing, respectively), followed by the neural network (with 99.75% and 99.5%), Gaussian classifier (with 99% and 98.75%), and PCA (with 25.25%). Thus, the supervised learning algorithms presented better results than the unsupervised learning classifier based on PCA.

For the experimental results, the low overall success rates obtained by PCA were 25% and 25.25% for the sinusoidal and triangular magnetic strength. The best results were obtained using the Gaussian classifier (with 99.75% and 99.5% success for training and testing, respectively), followed by neural network (with 99.25% and 99%) and KL transformation (with 97% and 96.5%), while for triangular magnetic strength, the best results were obtained using KL transformation (with 99.25% and 98.25% success for training and testing, respectively), followed by the neural network (with 99% and 99%) and the Gaussian classifier (with 98.75% and 98.75%). Like in the computational results, the supervised learning algorithms presented better results than PCA. The results also indicate that the triangular external excitation improves the performance of the classifiers.

The results obtained show the efficiency of the electromagnetic sensor in recognizing the diameters of the studied rebars. However, it does not show the effectiveness of this analysis when the bars have depths equal to or greater than 20 mm, so it is necessary to improve the sensor and use more information contained in the hysteresis loops for the characterization of the different rebar diameters.

References

1. Smith, W.: Structure and Properties of Engineering Alloys. McGraw-Hill, New York (1993)
2. Verma, S.K., Bhadauria, S.S., Akhtar, S.: Review of nondestructive testing methods for condition monitoring of concrete structures. J. Constr. Eng. (Hindawi). **2013**, 1–11 (2013). https://doi.org/10.1155/2013/834572
3. Rumiche, F., Indacochea, J.E., Wang, M.L.: Detection and monitoring of corrosion in structural carbon steels using electromagnetic sensors. J. Eng. Mater. Technol. **130**, 1–7 (2008). https://doi.org/10.1115/1.2931145
4. Rens, K.L., Wipf, T.J., Klaiber, F.W.: Review of nondestructive evaluation techniques of civil infrastructure. J. Perform. Constr. Facil. **11**, 152–160 (1997). https://doi.org/10.1061/(ASCE)0887-3828(1997)11:4(152)
5. Scheel, H., Hillemeier, B.: Capacity of the remanent magnetism method to detect fractures of steel in tendons embedded in prestressed concrete. NDT&E Int. **30**, 211–216 (1997). https://doi.org/10.1016/S0963-8695(96)00058-8
6. Scheel, H., Hillemeier, B.: Location of prestressing steel fractures in concrete. J. Mater. Civil Eng. **15**, 228–234 (2003). https://doi.org/10.1061/(ASCE)0899-1561(2003)15:3(228)
7. Mihalache, O., Pedra, G., Yusa, N., Miya, K.: Experimental measurements and numerical simulation of ID and OD signals in plate ferromagnetic materials using magnetic flux leakage. In: Gottvald, A. (ed.) Proceedings of the 4th Japan-Central Europe Joint Workshop on Energy and Information in Non-linear Systems. pp. 1–5. Energy and Information in Non-Linear Systems, Brno, CR (2001)
8. Sawade, G., Krause, H.J.: Magnetic flux leakage (MFL) for the non-destructive evaluation of pre-stressed concrete structures. In: Maierhofe, C., Reinhardt, H.W., Dobmann, G. (eds.) Non-destructive Evaluation of Reinforced Concrete Structures, pp. 215–242. WP, Cambridge (2010)
9. Fernandes, B., Wade, J.D., Nims, D.K., Devabhaktuni, V.K.: A new magnetic sensor concept for nondestructive evaluation of deteriorated prestressing strand. Res. Nondestruct. Eval. **23**, 46–68 (2012). https://doi.org/10.1080/09349847.2011.626143
10. Fernandes, B., Titus, M., Nims, D.K., Ghorbanpoor, A., Devabhaktuni, V.K.: Practical assessment of magnetic methods for corrosion detection in an adjacent precast, prestressed concrete box-beam bridge. Nondestr. Test. Eval. **28**, 99–118 (2013). https://doi.org/10.1080/10589759.2012.695785
11. Jiles, D.C., Atherton, D.L.: Theory of ferromagnetic hysteresis. J. Magn. Magn. Mater. **61**, 48–60 (1986)
12. Rumiche, F., Indacochea, J.E., Wang, M.L.: Assessment of the effect of microstructure on the magnetic behavior of structural carbon steels using an electromagnetic sensor. JMEPEG. **17**, 586–593 (2008). https://doi.org/10.1007/s11665-007-9184-2
13. Wang, X., Chen, J.G., Su, G.F., Cui, C., Li, H.Y.: Application of electromagnetism method to characterize the degradation behavior in structural mild steel within the elastic range. Constr. Build. Mater. **241**, 1–9 (2020). https://doi.org/10.1016/j.conbuildmat.2020.118011
14. Weiss, P.: L'hypothèse du champ moléculaire et la propriété ferromagnétique. J Phys (1907). https://doi.org/10.1051/jphystap:019070060066100
15. Cullity, B.D., Graham, C.D.: Introduction to Magnetic Materials. Wiley, Hoboken (NJ) (2009)
16. Szynowski, J., Kolano, R., Kolano-Burian, A., Varga, L.K.: Dynamic magnetic properties of the Fe-based alloys under non-sinusoidal excitation. J. Magn. Magn. Mater. (2008). https://doi.org/10.1016/j.jmmm.2008.04.057
17. COMSOL: COMSOL Multiphysics, https://br.comsol.com/learning-center/add-predefined-materials-comsol-multiphysics, (2019)
18. Reitz, J.R., Milford, F.J.: Foundations of Electromagnetic Theory. Addison Wesley, Boston (1962)
19. Mammadov, J.: Models of simple iron cored electromagnets. In: Proceedings of the 2014 COMSOL Conference. pp. 1–7. COMSOL, Cambridge (2014)
20. ASTM B258: Standard specification for standard nominal diameters and cross-sectional areas of AWG sizes of solid round wires used as electrical conductors. West Conshohocken (2018)
21. Webb, A.R.: Statistical pattern recognition. Wiley, Chichester (2002)
22. da Silva, F.E., Freitas, F.N.C., Abreu, H.F.G., Gonçalves, L.L., de Moura, E.P., Silva, M.R.: Characterization of the evolution of recrystallization by fluctuation and fractal analyses of the magnetic hysteresis loop in a cold rolled non-oriented electric steel. J. Mater. Sci. **46**, 3282–3290 (2011). https://doi.org/10.1007/s10853-010-5215-8
23. Vieira, A.P., de Moura, E.P., Gonçalves, L.L.: Fluctuation analyses for pattern classification in nondestructive materials inspection. EURASIP J. Adv. Sig. Process. (Hindawi). **2010**, 1–12 (2010). https://doi.org/10.1155/2010/262869
24. de Moura, E.P., Junior, F.E., Damasceno, F.F., Figueiredo, L.C., de Andrade, C.F., de Almeida, M.S., Rocha, P.A.: Classification of imbalance levels in a scaled wind turbine through detrended fluctuation analysis of vibration signals. Renew Energy. **96**, 993–1002 (2016). https://doi.org/10.1016/j.renene.2016.05.005
25. Haykin, S.: Neural Networks and Learning Machines. Pearson, Upper Saddle River (2009)